RSC Advances

ROYAL SOCIETY OF CHEMISTRY

www.rsc.org/advances

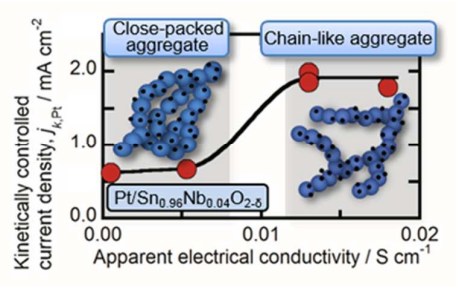

We found the specific activities of $Pt/Sn_{0.96}Nb_{0.04}O_{2-\delta}$ for the oxygen reduction reaction increased with increasing conductivity of the support.

RSC Advances

RSCPublishing

ARTICLE

Improvements in electrical and electrochemical properties of Nb-doped $SnO_{2-\delta}$ supports for fuel cell cathodes due to aggregation and Pt loading

Cite this: DOI: 10.1039/x0xx00000x

Received 00th January 2012,
Accepted 00th January 2012

DOI: 10.1039/x0xx00000x

www.rsc.org/

Yuichi Senoo,[a,c] Katsuyoshi Kakinuma,[a*] Makoto Uchida,[a**] Hiroyuki Uchida,[a,b] Shigehito Deki[a] and Masahiro Watanabe[a***]

We found that Nb-doped $SnO_{2-\delta}$ nanoparticles were improved in their electrical conductivity by more than two orders of magnitude by the aggregation of the particles, including the fusion of nearest-neighbor particles to form a random branching structure, and the formation of a porous agglomerated structure similar to that of conventional carbon blacks. The electrical conductivity was increased by an additional two orders of magnitude as a result of the loading of Pt nanoparticles to produce an electrocatalyst (Pt/Nb-doped $SnO_{2-\delta}$) for fuel cell applications. We also found that the specific activities of $Pt/Sn_{0.96}Nb_{0.04}O_{2-\delta}$ (16 wt% Pt loading) for the oxygen reduction reaction increased with increasing electrical conductivity of the support and exceeded that of a conventional Pt catalyst supported on carbon black (Pt/CB). Since the tin oxide supports are much more stable than CB supports to the exposure to positive potentials (0.9 ~ 1.3V) during the start/stop operation of fuel cells, Pt or Pt alloy catalysts supported on oxide supports with such a chain-like, necked structure, as developed in this work, become superior candidates as robust cathode catalysts for the fuel cell vehicle application.

a. Fuel Cell Nanomaterials Center, University of Yamanashi, Miyamae 6-43, Kofu, 400-0021, Japan.
b. Clean Energy Research Center, University of Yamanashi, Takeda 4, Kofu, 400-8511, Japan.
c. Mitsui Mining and Smelting Co., Ltd., Haraichi 1333-2, Ageo, Saitama, 362-0021, Japan.
Author to whom correspondence should be addressed.
* Phone: +81-55-254-7143; Fax: +81-55-254-7143
E-mail: kkakinuma@yamanashi.ac.jp
** Phone: +81-55-254-7095; Fax: +81-55-254-7095
E-mail: uchidam@yamanashi.ac.jp,
***Phone: +81-55-220-8620; Fax: +81-55-254-0371;
E-mail: m-watanabe@yamanashi.ac.jp

1 Introduction

Polymer electrolyte fuel cells (PEFCs) are highly attractive power generation systems for fuel cell vehicles and residential co-generation systems, with low emissions and high energy efficiency. Carbon-supported Pt is one of the principal candidates as a catalyst for the cathode, although the degradation of the carbon support remains a significant problem.

Carbon has an intrinsic thermodynamic instability as a result of its oxidative corrosion to carbon dioxide (eq. 1) under the typical PEFC operating condition of low pH and high humidity.[1,2]

$$C + 2H_2O \rightarrow CO_2 + 4H^+ + 4e^-;\ E^0 = 0.207\ V\ vs.\ RHE \quad (1)$$

Operation in the higher potential range (> 0.9 V), particularly under automotive start/stop conditions, accelerates the degradation of the cathode catalyst and leads to the deterioration of the PEFC performance.

The development of alternative supports to carbon with high electrical conductivity and stability in the high potential range is very important to ensure the success of fuel cell commercialization, and a number of candidates have been reported, such as Pt/TiO_2,[3] Pt/TiB,[4] Pt/TiN,[5] Pt/In_2O_3-SnO_2,[6] Pt/Ti_4O_7,[7] Pt/WO_3,[8] Pt/TiC,[9] Pt/WC[10] and Pt/IrO_2.[11] In particular, Pt catalysts supported on Magneli phase Ti_4O_7 and TiO_x were reported to be stable at high potentials (< 1.5 V), and a single cell with a 10 wt % Pt catalyst supported on a Ti_4O_7 cathode was operated (80°C at 0.67 V with H_2/O_2) successfully for 350 h.[12-14] Pt/Sb-doped $SnO_{2-\delta}$ and Pt/Nb-doped $SnO_{2-\delta}$ have also been proposed to be promising long-term, durable cathode

materials at high potential.[15-18] In our previous paper, the solubility of tin oxide in ORR condition was reported to be quite small.[19] The solubility of $Pt/Sn_{0.96}Nb_{0.04}O_{2-\sigma}$ in 0.1 mol dm^{-3} H_2SO_4 aqueous solutions at 80 °C under reducing conditions (H_2 bubbling) and oxidizing conditions (air bubbling) were investigated. The Sn-cation (Sn^{2+}) content in the solution was 0.21×10^{-8} mol $mg_{(support)}^{-1}$ after three weeks, and Nb was not detected. The value corresponded to 0.033 atom% Sn in the $Sn_{0.96}Sb_{0.04}$ $O_{2-\sigma}$ support. The electrochemically active surface area (ECSA) and electrochemical activity of Pt supported on these non-carbon supports have often been reported to be much lower than those of Pt catalysts supported on carbon. However, we reported that a Pt catalyst supported on TiN (Pt/TiN) showed both higher mass activity and ECSA values than those of Pt catalysts supported on carbon.[20] The Pt catalyst particles were found to be highly oriented in relation to the lattice structure of the TiN support particles, without any additional phases at the Pt/TiN interface, presumably enhancing the electronic contact and leading to the high oxygen reduction performance of the Pt/TiN.

Alternative non-carbon supports also require high surface area to maintain a high dispersion of the Pt nanoparticles. Mesoporous particles,[21,22] nanoparticles,[23,24] nanotubes[25] and nanowires[26] have been reported as preferred microstructures to construct high surface area supports. In addition, the electrocatalyst of the PEFC is necessarily in the form of a gas diffusion electrode, which requires not only a high surface area but also an electrically conductive path and a gas diffusion path. To meet these requirements, we proposed an Nb-doped $SnO_{2-\delta}$ nanoparticle support with aggregated network structure to be applied in PEFC cathodes.[19,27] The aggregated network structure, including fusion of nearest-neighbor particles to form a random branching structure, is similar to that of carbon black. A single cell using such an aggregated Nb-doped $SnO_{2-\delta}$-supported Pt catalyst showed higher cathodic activity than that using a carbon black-supported Pt catalyst.

In the present work, we seek to characterize and explain in more detail the attractive features of these types of novel supports and catalysts. For example, the electrical conductivity of nanoparticles with an aggregated network structure is anticipated to be enhanced with the development of a branched structure from the results of computational simulations.[28] The oxygen reduction reaction of the gas diffusion electrode is strongly dependent on the electron transport capacity of electronically conductive paths. In the present paper, we report an investigation of the relationship of the electronic conductivity, microstructure of Nb-doped $SnO_{2-\delta}$, and the oxygen reduction reaction activity of Pt/Nb-doped $SnO_{2-\delta}$, and have elucidated the appropriate aggregated network structure of the latter, which showed higher oxygen reduction reaction activity compared to that of a commercial carbon-supported Pt catalyst.

2 Experimental

We synthesized the Nb-doped $SnO_{2-\delta}$ support, with an aggregated network structure similar to that of carbon black (CB), by a flame oxide-forming method.[19,27] Tin 2-ethylhexanoate $Sn(C_7H_{15}COO)_4$ and niobium 2-ethylhexanoate $Nb(C_7H_{15}COO)_5$ were used as starting materials. These materials were mixed at the desired mole ratio and were dissolved in terpene oil or 2-ethylhexanoic acid. These solutions were mixed by use of a magnetic stirrer for 2 h at room temperature. The obtained solutions were supplied to an atomizer at a rate of 1.4~3.4 g min^{-1} by a peristaltic pump and were injected into a flame with oxygen gas at a rate of 9 L min^{-1}. The temperature of the flame, which was generated by propane (1 L min^{-1}) and oxygen (5 L min^{-1}), was about 1400°C, as measured by an infrared-ultraviolet radiation thermometer (IR-CAQ2CS, Chino Co.). The gas flow rates mentioned above were maintained constant for all samples to unify the oxidation conditions The entire oxidation reaction lasted for about one hour, and ca. 10 g of powder was collected with a high efficiency particulate air (HEPA) filter. Pt nanoparticles were loaded on the Nb-doped $SnO_{2-\delta}$ by a colloidal method.[29-31] The as-prepared catalysts were heat-treated at 150 °C in a 1 %-H_2 (balance N_2) atmosphere for 2 h and quenched to room temperature under the same atmosphere

Crystallographic structures and crystallites sizes of the obtained Nb-doped $SnO_{2-\delta}$ were confirmed by X-ray diffraction measurements (XRD, Ultima 4, Rigaku Co.) with Cu Kα radiation (0.15406 nm, 40 kV, 40 mA). The crystallite size of the Nb-doped $SnO_{2-\delta}$ particles was also evaluated with XRD by examining the peak at 2θ~33.9°.

The morphology of the catalysts and support materials was observed by transmission electron microscopy (TEM, H-9500, Hitachi High-Technologies Co.). The average particle diameters and size distributions of the Pt nanoparticles were also estimated from the TEM images.

The surface area of the oxide support was estimated by the Brunauer, Emmett and Teller absorption method (BET, BELSORP-max, Nippon BEL Co.). The amount of the supported Pt catalyst and chemical composition of Sn and Nb in the support were quantitatively analyzed by use of an inductively coupled plasma-mass spectrometric analyzer (ICP-MS, 7500CX, Agilent Technologies Inc.). The analysis of the Pt content was carried out with aqueous solutions that were prepared by the dissolution of the Pt catalysts in hot aqua regia. The analysis of Sn and Nb was carried out with an aqueous hydrochloric acid solution, which was prepared after a pretreatment of the support by the alkaline fusion method (sodium carbonate and sodium peroxide).

The apparent electrical conductivity measurement was performed under ambient air atmosphere with the two probe method. The support powders were placed into a cylinder with a radius of 1 cm, and aluminum foil electrodes were placed at the top and bottom of the column of support powder. The electrical resistance was measured under an applied pressure (19 MPa) with a DC resistivity analyzer (Ohm Tester Model 3565, Tsuruga Electric Co.). The apparent electrical resistivity

of the sample was estimated from the slope of the relationship between resistance and sample thickness.

The pore size distribution of the support particles was measured by mercury intrusion porosimetry (AutoPore IV 9520, Micromeritics Co.) to evaluate the pore volume and variation of the network structure of the $Sn_{0.96}Nb_{0.04}O_{2-\delta}$. The mercury intrusion pressure was applied from 3.0×10^{-3} MPa to 4.1×10^{2} MPa. The intrusion curves showed two pore-size distributions with a boundary pore-size of ca. 30 nm, where the smaller pores, defined as primary pores, formed between the aggregated oxide particles, and larger ones as secondary pores, formed between the agglomerates of the aggregates, in the same manner as for conventional CB structures.[32]

A cyclic voltammetric (CV) measurement for the determination of electrochemical surface area (ECSA) and a linear sweep voltammogram for the measurement of the oxygen reduction reaction (ORR) activity were performed with the rotating disk electrode (RDE), respectively. The catalyst was uniformly dispersed on the glassy carbon substrate (RDE electrode, 5 mm in diameter) by delivering an appropriate amount of a mixed solution of ethanol and water (9:1 volume ratio), in which the catalyst was suspended, for a constant loading of Pt, 11 μg cm^{-2}. Then, a suspension of 5 wt% Nafion® diluted with a mixed solution of ethanol and water (9:1 volume ratio) was spread evenly over the catalyst layer to yield an average film thickness of 50 nm. The Nafion® coated electrode was dried in air under a high ethanol vapor pressure at room temperature for 12 h. The counter electrode was a platinum wire. The potential of the working electrode was referenced to a reversible hydrogen electrode (RHE) immersed in the same solution. The electrolyte solution of 0.1 M $HClO_4$ was prepared from reagent grade chemicals (Kanto Chemical Co.) and Milli-Q water (ultrapure water, 18.2 MΩ cm, Milli-Pore Japan Co.). A potentiostat (HZ-5000, Hokuto Denko Co.) was used for the CV and linear sweep voltammetry (LSV) measurements. Before carrying out the CV measurement, the catalyst dispersed on the RDE electrode were subjected to 60 potential cycles from 0.05 V to 1.15 V vs. RHE at a sweep rate of 0.2 V s^{-1} to remove impurities from the surface of the catalyst. After these potential cycles, the electrolyte solution was replaced with fresh solution. The CV was recorded by sweeping the potential from 0.05 to 1.0 V vs. RHE at 0.1 V s^{-1} at 25◦C. The electrolyte solution was purged with N_2 gas for at least 1 h prior to the CV measurements. The ECSA of Pt was evaluated from the electrical charge for the hydrogen adsorption (Q_H) in the negative-going potential sweep from 0.40 to 0.05 V in the CV at a sweep rate of 0.1 V s^{-1}, after subtraction of the double layer charge (Q_{DL}),[32] assuming Q_H = 0.21 mC cm^{-2}, conventionally adopted for smooth polycrystalline platinum.[33,34] The ORR measurement was conducted by LSV, sweeping the potential from 0.25 to 1.0 V vs. RHE at 5 mV s^{-1} at rotation rates in the 1000-2750 rpm range at 25 °C. The electrolyte solution was saturated with O_2 gas by purging for at least 1 h prior to the measurements.

3 Results and discussion

3.1 Characterization of $Sn_{0.96}Nb_{0.04}O_{2-\delta}$ support and $Pt/Sn_{0.96}Nb_{0.04}O_{2-\delta}$ catalyst

The XRD pattern of a $Sn_{0.96}Nb_{0.04}O_{2-\delta}$ support powder representative of the eleven powder samples synthesized by the flame oxide synthesis method is shown in Fig. 1.

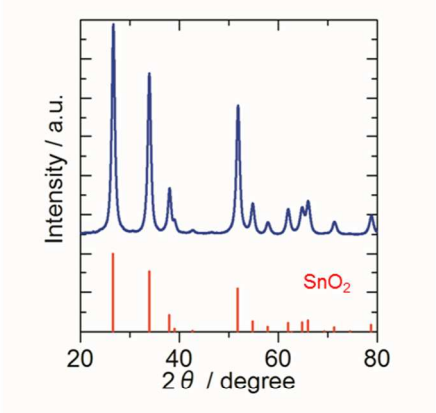

Fig. 1. X-ray diffraction pattern for $Sn_{0.96}Nb_{0.04}O_{2-\delta}$. All peaks were assigned to those of rutile-type $SnO_{2-\delta}$ without any impurity phase such as Nb_2O_5. The XRD profile of rutile-type $SnO_{2-\delta}$ (International Centre for Diffraction Data, Powder Diffraction File (ICDD PDF):01-088-0287) is also displayed for reference.

All peaks were assigned to those of rutile-type $SnO_{2-\delta}$, without any impurity phase such as Nb_2O_5. We did not detect a clear peak shift, so there is no direct XRD evidence for Nb-doping; this could perhaps be expected, since the ionic radii of Sn^{4+} (0.69Å) and Nb^{5+} (0.64Å), for the case of a coordination number of six, are quite similar.[35] The Nb concentration was determined to be Sn:Nb = 0.96:0.04 (mol%, $Sn_{0.96}Nb_{0.04}O_{2-\delta}$) from the ICP-MS result. The BET surface areas of the obtained powders ranged from 37 m^2 g^{-1} to 105 m^2 g^{-1}. We considered the electrical conductivity of these nanoparticles to be strongly influenced by necking between nanoparticles. We evaluated the level of necking between nanoparticles with a "necking index" (NI= S_{BET}/ S_{XRD}), defined by the ratio of the specific surface area measured by the conventional BET method (S_{BET}) to the surface area estimated by assuming a spherical shape in a non-necked state, with the mean crystallite size determined by the XRD method (S_{XRD}). A decrease of the value below NI= 1.0 indicates the development of necking compared with the separated particle state. The oxide nanoparticles exhibited NI values from 0.91 to 0.67, indicating the presence of nanoparticles aggregated to various extents. Figure. 2 (a)-(b) shows TEM images for typical nanoparticles with different NI values, 0.91 and 0.83, respectively. The former (a) appears to have a close-packed aggregated structure and the latter (b) a chain-like aggregated structure. It is clear from the high resolution TEM image of Fig. 2(c) that each oxide nanoparticle was made up of well crystallized particles, without any amorphous layer, which could have been detected by in a phase contrast images.[27] We also detected the lattice plane of (101) in Fig. 2(d). The existence of these high-quality crystallites relies

on the high temperature (1400°C) sintering in the flame oxide-forming method. More over the obtained particles consisted of necked particles, with diameters ranging from about 10 nm to 30 nm, forming an aggregated network structure and primary pores, as defined below in the Experimental Section, similar to that of carbon blacks.[32] The development of necking, comparing state (a) and (b) in Fig. 2, brought about an increase of the primary pore volume, i.e., 0.165 mL g^{-1} to 0.215 mL g^{-1}. We considered that the aggregation of the oxide nanoparticles, which correlated quantitatively with the NI values and pore volume, must change the electronic conductivity and also the electrocatalytic activity for the ORR.

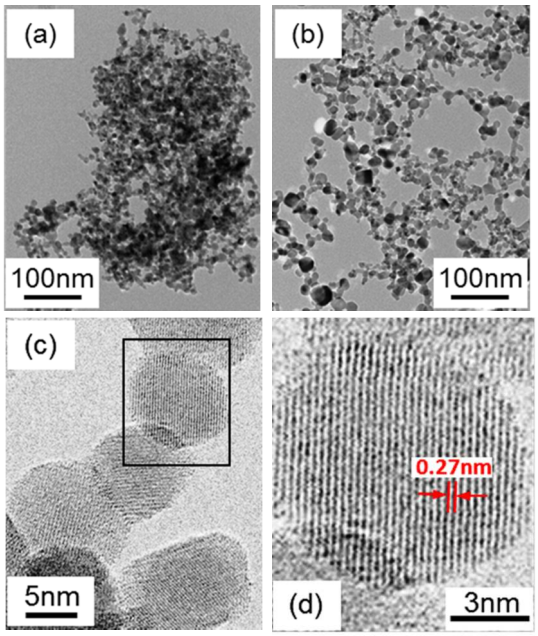

Fig. 2. Transmission electron microscopy image of $Sn_{0.96}Nb_{0.04}O_{2-\delta}$ particles: (a) close-packed aggregated type (sample (A), NI 0.91, primary pore volume 0.165 mL g^{-1}), (b) chain-like aggregated type (sample (E), NI 0.83, primary pore volume 0.215 mL g^{-1}), (c) high resolution TEM image of the $Sn_{0.96}Nb_{0.04}O_{2-\delta}$ particles (sample (E)), (d) lattice fringe analysis of the $Sn_{0.96}Nb_{0.04}O_{2-\delta}$ particles located in the square (Fig. 2(c)).

The apparent electrical conductivity of the obtained nanoparticles was plotted as a function of the value of NI and the volume of the primary pores, respectively, in Fig. 3(a) and (b). The values of electronic conductivity were from 5.9 × 10^{-7} to 2.0 × 10^{-4} S cm^{-1}; these were much higher than that of Nb-free tin oxide (5.5 × 10^{-9} S cm^{-1}, NI: 0.81, primary pore volume 0.19) prepared by the same synthesis conditions as those of sample C. We consider that this result indicates Nb-doping

In Fig. 3(a), we found that the apparent electrical conductivity of the nanoparticles generally increased with increasing NI but exhibited two distinctly different types of dependence, e.g., onetype including samples B and D, and a second type including samples C and E, shown in the figure. A very interesting discovery was that the enhancement of the electrical the NI value for sample E was much higher than that for sample D. Figure 3(b) clearly shows that the electrical conductivity increased with increasing primary pore volume. The electrical conductivity of a porous material has a tendency to increase with the development of an aggregated network structure, also accompanied by an increase of the primary pore volume, due to the network being formed with non-linear aggregation.[28,32]

We also found that the microstructure of the $Sn_{0.96}Nb_{0.04}O_{2-\delta}$

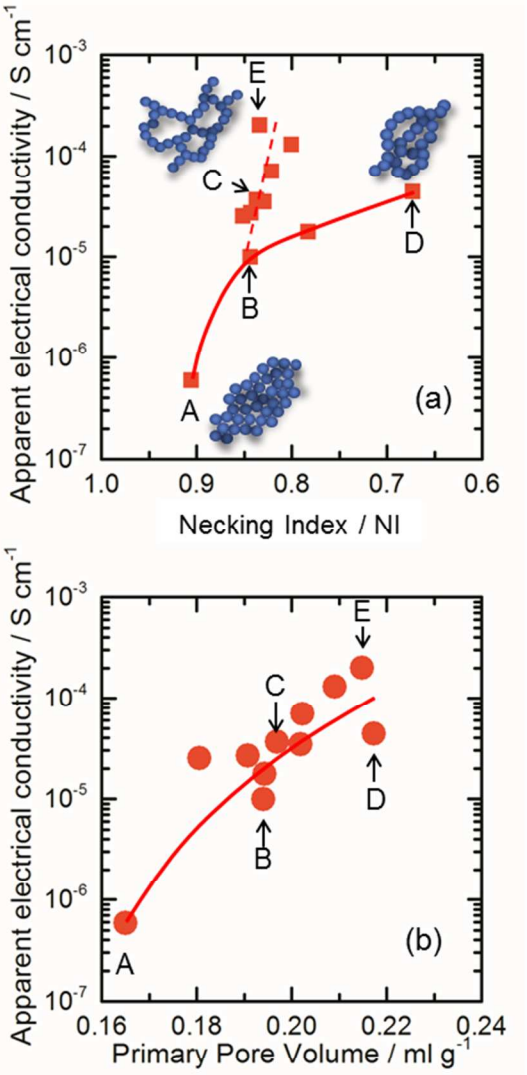

Fig. 3. Apparent electrical conductivities of $Sn_{0.96}Nb_{0.04}O_{2-\delta}$ particles as a function of necking index (a) and primary-pore volume (b), where the symbols A-E indicate the oxide supports used for further studies below as Pt supported on sample A-E. Schematic drawings in Fig. 3(a) are artistic representations of the respective aggregated network samples.

nanoparticles changed from a close-packed, aggregated type to a chain-like, aggregated type with increasing primary pore volume, as seen in Fig. 2(a)-(b) and Fig. 3(a)-(b). These results indicate that the chain-like aggregated structure would be preferable for the PEFC electrode. Therefore, we selected several of the $Sn_{0.96}Nb_{0.04}O_{2-\delta}$ support powders (samples A-E) shown in Fig. 3 and deposited Pt catalyst nanoparticles on them (denoted as $Pt/Sn_{0.96}Nb_{0.04}O_{2-\delta}$). The Pt nanoparticles were highly dispersed over the surface on each support, as shown in the TEM images (Fig. 4).

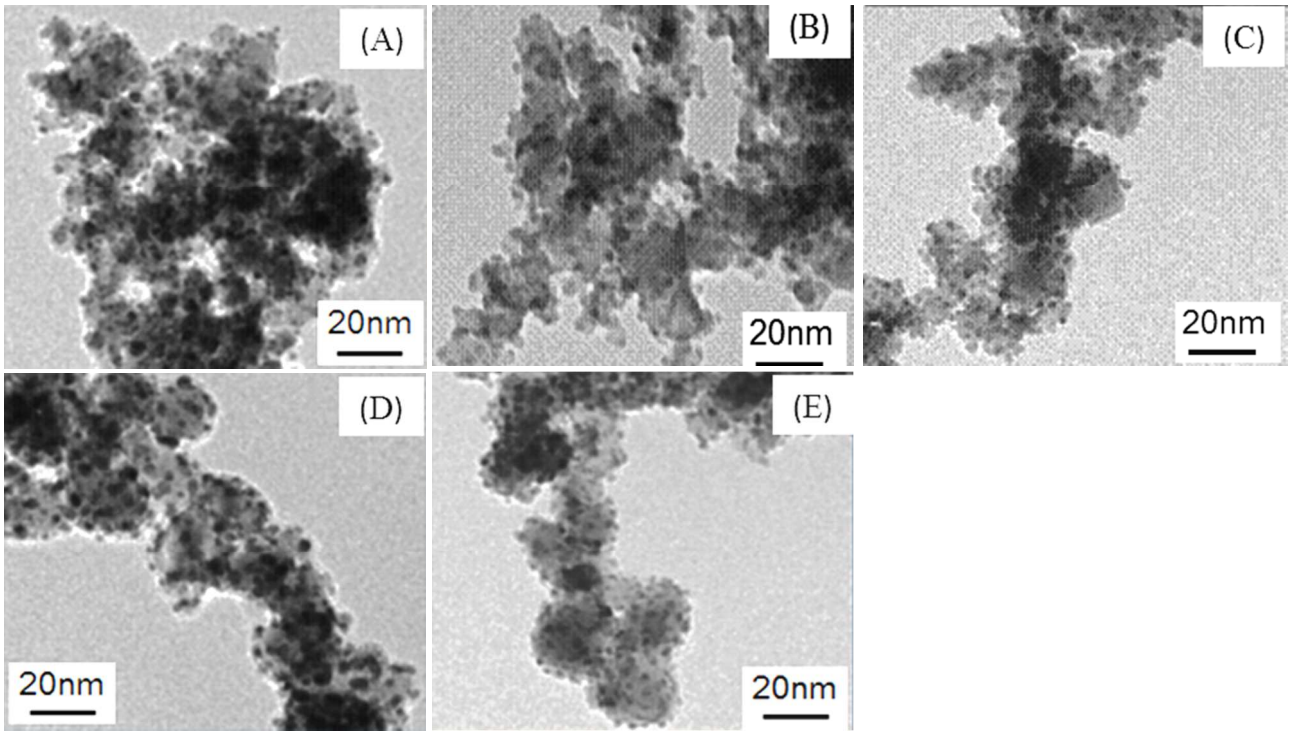

Fig. 4. Transmission electron microscopic images of $Pt/Sn_{0.96}Nb_{0.04}O_{2-\delta}$ particles: (A) sample A, (B) sample B, (C) sample C, (D) sample D, (E) sample E. The notation (A to E) corresponds to that of Tables 1 and 2.

Table 1. Pt loading, Pt particle size, and Pt intercrystallite distance of Pt nanoparticles supported on the $Sn_{0.96}Nb_{0.04}O_{2-\delta}$ ($Pt/Sn_{0.96}Nb_{0.04}O_{2-\delta}$) after heat treatment at 150 °C in 1% H_2 atmosphere for 2 h. Five $Sn_{0.96}Nb_{0.04}O_{2-\delta}$ supports with various aggregated network structures, which were designated samples A, B, C, D, E, are shown in Fig. 3. $\sigma_{app.}$ is defined as an apparent electrical conductivity measured under compression (19 MPa) and under an ambient air with the two probe method.

Oxide Support	Primary pore Volume / ml g^{-1}	$\sigma_{app.}$ without Pt loading / S cm^{-1}	$\sigma_{app.}$ with Pt loading / S cm^{-1}	Pt loading / wt %	Pt particle size / nm	Pt-Pt distance / nm
A	0.165	5.9×10^{-7}	5.2×10^{-4}	15.2	2.6 ± 0.5	11.5
B	0.194	9.9×10^{-6}	5.3×10^{-3}	17.3	3.0 ± 0.5	10.8
C	0.197	3.7×10^{-5}	1.3×10^{-2}	16.9	2.9 ± 0.5	10.0
D	0.217	4.4×10^{-5}	1.8×10^{-2}	16.9	3.1 ± 0.5	8.3
E	0.215	2.0×10^{-4}	1.3×10^{-2}	16.9	3.0 ± 0.5	9.2

The Pt particle sizes and the amounts of Pt loading were also controlled within a narrow range (particle diameter, 2.6 ± 0.5 nm to 3.1 ± 0.5 nm; Pt loading, 15.2 wt % to 17.3 wt %) for each catalyst, regardless of the differences in NI or the primary pore volume. The distances between Pt nanoparticles were controlled to be within the range of 8.3 to 11.5 nm (Table 1).

The apparent electrical conductivities of the Pt-loaded oxide catalysts under air are plotted as a function of the primary pore volume of these supports in Fig. 5, together with the conductivities for the corresponding oxide supports without Pt loading (samples A-E), taken from Fig. 3. We found that the apparent electrical conductivities of the Pt-supported catalysts were enhanced greatly, by more than two orders of magnitude compared to those of the supports alone. These $Pt/Sn_{0.96}Nb_{0.04}O_{2-\delta}$ catalysts and $Sn_{0.96}Nb_{0.04}O_{2-\delta}$ supports were heat-treated under the same conditions described in the Experimental section, and had the same content of aliovalent cation dopant. The electrical conductivity of nanometer-sized metal oxide particles tends to be influenced in general by the presence of adsorbed molecules,[36,37] as will be discussed in the next section.

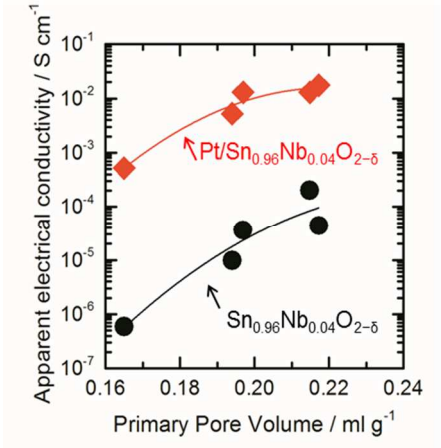

Fig. 5. Apparent electrical conductivities of $Sn_{0.96}Nb_{0.04}O_{2-\delta}$ particles and Pt/ $Sn_{0.96}Nb_{0.04}O_{2-\delta}$ particles in air atmosphere plotted with primary pore volumes, where the former group

3.2 Conducting mechanism of Pt/$Sn_{0.96}Nb_{0.04}O_{2-\delta}$ catalyst and $Sn_{0.96}Nb_{0.04}O_{2-\delta}$ support with aggregated network structure.

As a factor that sensitively affects the electrical conductivity of tin oxide, the effect of chemisorbed, charged oxygen species (O_2^-, O^-, O^{2-}) can be generated by the reduction of oxygen molecules by electrons supplied from the tin oxide. [36,37] Therefore, we examined in more detail the sensitivity of the electronic conductivity of the $Sn_{0.96}Nb_{0.04}O_{2-\delta}$ powders with/without Pt loading under various gas atmospheres. The representative sample powders, taken from sample C with /without Pt, were pressed into a rectangular shape and were pre-treated at 150 °C under argon for 1.5 h in order to desorb the adsorbed molecules on the surface, following a reported procedure,[37] and then cooled in an argon atmosphere. Then, the atmosphere was replaced with pure oxygen for 3 h and then replaced by argon again, as shown by the sequence of temperature and atmosphere treatments in Fig. 6(a).

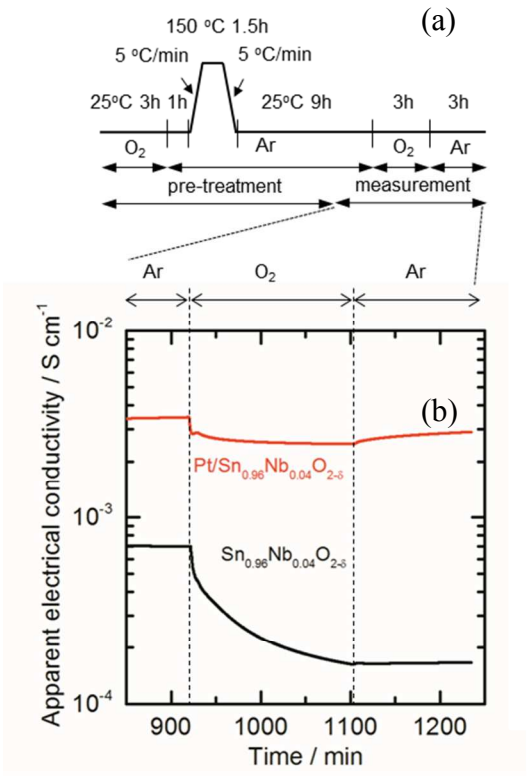

Fig. 6. Apparent electrical conductivity of $Sn_{0.96}Nb_{0.04}O_{2-\delta}$ and Pt/$Sn_{0.96}Nb_{0.04}O_{2-\delta}$ monitored under Ar and O_2 atmospheres. (a) the sequence shows the temperature and atmosphere during the heat treatment and conductivity measurements, (b) variation of the apparent electrical conductivity of $Sn_{0.96}Nb_{0.04}O_{2-\delta}$ and Pt/$Sn_{0.96}Nb_{0.04}O_{2-\delta}$ by changing atmospheric conditions. Each sample was pre-treated at 150 °C in argon and cooled to room temperature under the same atmosphere, without exposure to the ambient atmosphere.

During this sequence, the electrical conductivities at 25°C were monitored without exposure to the ambient atmosphere. The results are shown in Fig.6(b). We found an abrupt but slight decrease of the electrical conductivity at Pt/$Sn_{0.96}Nb_{0.04}O_{2-\delta}$ as the atmosphere was changed to oxygen, but the conductivity recovered slowly after changing back to an argon atmosphere. However, the conductivity of the $Sn_{0.96}Nb_{0.04}O_{2-\delta}$ decreased markedly, reaching a value of only 25% compared to the initial value. It exhibited almost no recovery after changing from oxygen back to the argon atmosphere. Moreover, the electronic conductivity at Pt/$Sn_{0.99}Nb_{0.01}O_{2-\delta}$ powder increased with increasing amount of Pt loading, as shown in Fig. 7.

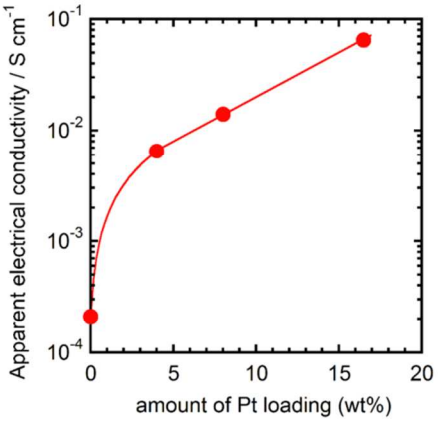

Fig. 7. Apparent electrical conductivities of Pt/$Sn_{0.99}Nb_{0.01}O_{2-\delta}$ particles in air atmosphere plotted vs. the Pt loading.

We consider that the Pt nanoparticles might lower the influence of adsorbed oxygen species on the charge carriers on the tin oxide nanoparticle surface. On the nano-sized tin oxide, chemisorbed molecules, such as charged oxygen species (O_2^-, O^-, O^{2-}), are generated by the reduction of oxygen molecules by electrons supplied from the tin oxide, thereby introducing a depletion layer, with band bending, on the surface of the oxide,[36] as shown in Fig. 8(a)-(b). This band bending in the depletion layer enhances the grain boundary resistance and interparticle resistance of nanoparticles, thus obstructing the electron conduction in the oxide.[37,38]

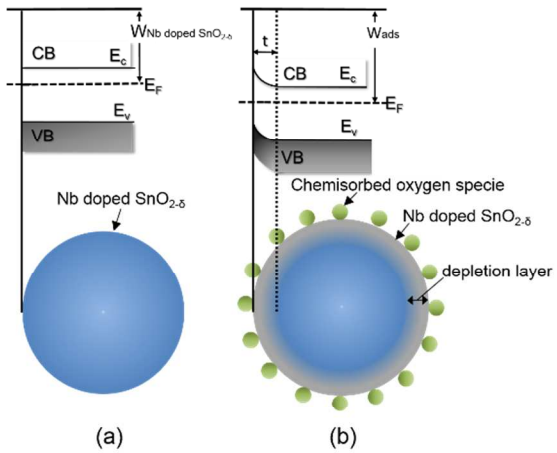

Fig. 8. Schematic band model of Nb-doped tin oxide: (a) Nb-doped tin oxide without chemisorbed oxygen species; (b) Nb-doped tin oxide with chemisorbed oxygen species; CB, conduction band; VB, valence band; E_C, conduction band minimum; E_F, Fermi level; E_V, valence band maximum; t, thickness of electron depletion layer; $W_{Nb\ doped\ tin\ oxide}$, work function of Nb-doped tin oxide; W_{ads}, work function of Nb-doped tin oxide after oxygen molecule adsorption; gray area, electron depletion layer of Nb-doped tin oxide particles; blue area, Nb-doped tin oxide particles without electron depletion layer.

The grain boundary and interparticle resistances decreased with the development of necking (Fig. 9(a)-(b)). [37] Moreover, our results (Fig. 6 (b)) indicate that Pt nanoparticles lowered the influence of adsorbed oxygen species on the $Sn_{0.96}Nb_{0.04}O_{2-\delta}$ nanoparticle surface, for example, by dissociating molecular oxygen, avoiding its reduction to superoxide, which would lead to the depletion of conduction electrons associated with the Nb dopant, by analogy with similar phenomena for titanium dioxide.[38] The result would be to shrink the depletion layer, along with the relief of band bending (Fig. 9(c)), and the suppression of the grain boundary and interparticle resistances. We will present further details, together with surface chemisorbed molecule characterization, carrier concentrations and oxygen vacancy concentrations, in the near future.

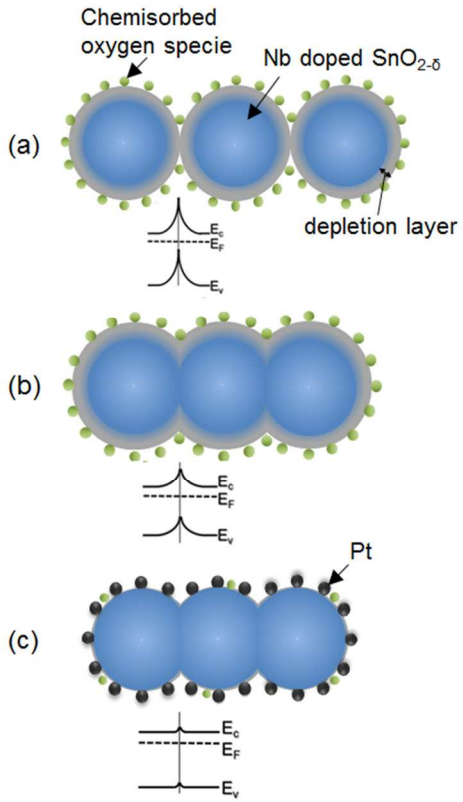

Fig. 9. Schematic model of depletion region for (a) Nb-doped tin oxide particles; (b) Nb-doped tin oxide particles with developed necking; and (c) Pt dispersed on Nb-doped tin oxide particles with developed necking. The depletion region around the interface between Nb-doped tin oxide particles disappears partially due to the necking, as shown, comparing (a) and (b). The depletion region also decreased due to Pt loading because of decreased amounts of charged species (c).

3.3 Electrochemical characterization of $Pt/Sn_{0.96}Nb_{0.04}O_{2-\delta}$ catalyst

Figure 10 shows the CVs for the $Pt/Sn_{0.96}Nb_{0.04}O_{2-\delta}$. RDEs in 0.1 M $HClO_4$ solution saturated with N_2 at 25 °C. The hydrogen adsorption/desorption peaks appear clearly. The ECSA values, which were evaluated based on the hydrogen adsorption on Pt particle surfaces, are listed in Table 2.

Anodic current due to oxide formation on the platinum surface also appeared above 0.7 V vs. RHE. These peak positions correspond well to those for the commercial Pt/CB or Pt/GCB for the similar potential sweep range (0.05 V to 1.0 V vs. RHE), as reported in previous work.[4] The inset in Fig. 11 shows the initial hydrodynamic voltammograms for the ORR for each $Pt/Sn_{0.96}Nb_{0.04}O_{2-\delta}$ sample, by the use of the RDE technique at 1750 rpm, in 0.1 M $HClO_4$ solutions saturated with oxygen at room temperature.

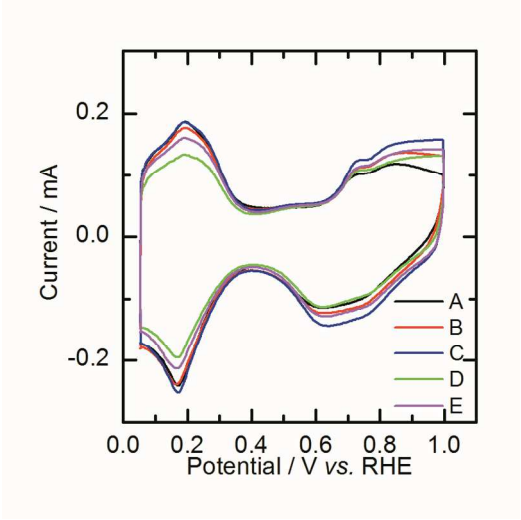

Fig. 10 Cyclic voltammograms for $Pt/Sn_{0.96}Nb_{0.04}O_{2-\delta}$ obtained at a sweep rate of 0.1 V s^{-1} in N_2-saturated 0.1 mol dm^{-3} $HClO_4$. The notation of A-E corresponds to that of Tables 1 and 2.

Table 2. The ECSA and the kinetically controlled current densities at 0.80 V on $Pt/Sn_{0.96}Nb_{0.04}O_{2-\delta}$ with different network-structure supports, A-E.

Sample	ECSA / $m^2 g^{-1}$	$j_{k,Pt}$ / mA cm^{-2}	Mass Activity / A g^{-1}
Pt/A	70.8	0.62	439
Pt/B	72.4	0.67	485
Pt/C	74.6	1.86	1387
Pt/D	59.4	1.79	1063
Pt/E	77.6	1.99	1544
Commercial Pt/CB[40)]	80.0	1.66	1328

The onset potentials for ORR at these catalysts were all ca. 0.98 V, and the ORR current approached the diffusion limiting value at around 0.5 V. The effect of the solution phase mass transport was removed with plots of the inverse current vs. the inverse of the square root of rotation rate ($\omega^{-1/2}$) obtained from these current-potential curves, based on the Koutecky-Levich equation[39]. Linear relationships with a constant slope were obtained at 0.8 V vs. RHE for the $Pt/Sn_{0.96}Nb_{0.04}O_{2-\delta}$ catalysts (Fig. 11). By extrapolating $\omega^{-1/2}$ to 0 (infinite mass transport rate), the kinetically controlled currents I_k were determined. Using these data, the kinetically controlled current densities based on real Pt area per unit geometric area ($j_{k,geo}/(A_{Pt}/A_{geo}) = j_{k,Pt}$) were determined. The $j_{k,Pt}$ values at 0.8 V for

$Pt/Sn_{0.96}Nb_{0.04}O_{2-\delta}$ increased with increasing apparent electrical conductivity of the $Pt/Sn_{0.96}Nb_{0.04}O_{2-\delta}$ catalyst and slightly exceeded that for a commercial Pt/CB catalyst [40] (Fig. 12). We consider that the aggregated network structure for the $Sn_{0.96}Nb_{0.04}O_{2-\delta}$ support, with well-dispersed Pt nanoparticles, is important for the development of electrocatalysts using electrically conductive ceramic nanoparticle supports for polymer electrolyte fuel cells in order to obtain Pt catalysts with high ORR activity.

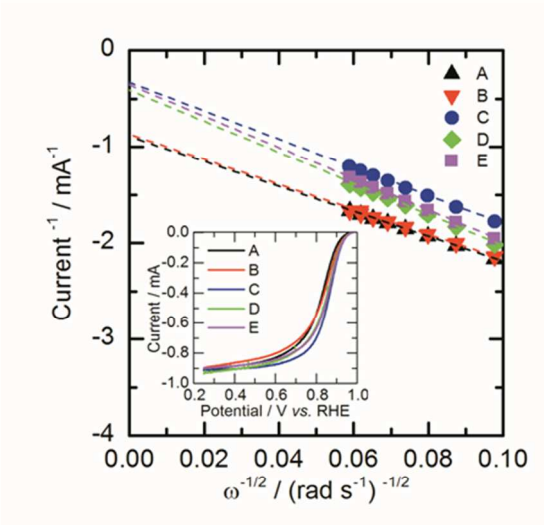

Fig. 11. Hydrodynamic voltammograms for the ORR on $Pt/Sn_{0.96}Nb_{0.04}O_{2-\delta}$, which were recorded by sweeping the potential from 0.05 to 1.00 V at 0.05 V s^{-1} at a rotation rate of 1750 rpm at room temperature. The notation of A-E corresponds to that of Tables 1 and 2.

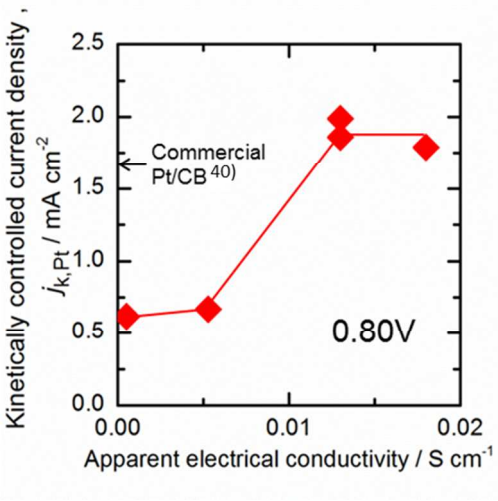

Fig. 12. Kinetically controlled current densities based on real Pt area of Pt/ $Sn_{0.96}Nb_{0.04}O_{2-\delta}$ at 0.80 V plotted as a function of the apparent electrical conductivities. The apparent electrical conductivity of a commercial Pt/CB catalyst (TEC10E50E, Tanaka Kikinzoku Kogyo Co.) was found to be 14 S cm^{-1} by use of the same measurement method.

4 Conclusions

We evaluated the electrical conductivity of $Sn_{0.96}Nb_{0.04}O_{2-\delta}$ nanoparticle supports with aggregated network structures similar to that of CB and the corresponding $Pt/Sn_{0.96}Nb_{0.04}O_{2-\delta}$ catalysts. The electrical conductivities of the $Sn_{0.96}Nb_{0.04}O_{2-\delta}$ nanoparticle supports increased strikingly, i.e., by two orders of magnitude, with increasing particle necking and primary pore volume, with the microstructure of the support progressing from a close-packed aggregated type to a chain-like aggregated type. We propose the formation of the electronically conducting paths constructed by the $Sn_{0.96}Nb_{0.04}O_{2-\delta}$ nanoparticles in the chain-like aggregates. Moreover, we found that the electrical conductivities of the $Pt/Sn_{0.96}Nb_{0.04}O_{2-\delta}$ samples measured at room temperature in air were enhanced further by more than two orders of magnitude compared to the corresponding $Sn_{0.96}Nb_{0.04}O_{2-\delta}$ supports without Pt loading. The electrical conductivity of $Pt/Sn_{0.96}Nb_{0.04}O_{2-\delta}$ was not as susceptible to oxygen as was the $Sn_{0.96}Nb_{0.04}O_{2-\delta}$ nanoparticle support. We consider that Pt nanoparticles might lower the influence of adsorbed oxygen species on the $Sn_{0.96}Nb_{0.04}O_{2-\delta}$ nanoparticle surface, which would relate to the improvement of the electrical conductivity of $Pt/Sn_{0.96}Nb_{0.04}O_{2-\delta}$. The electrochemical activity of the $Pt/Sn_{0.96}Nb_{0.04}O_{2-\delta}$ samples improved with increasing electrical conductivity and exceeded that of a commercial Pt catalyst supported on carbon black (Pt/CB). Thus, we conclude that both the development of necking between oxide nanoparticles by fusion of nearest-neighbor particles to form a random branching structure and the presence of well-dispersed Pt nanoparticles are preferred for the enhancement of the electrochemical activity.

Acknowledgements

This work was partially supported by funds for the "Research on Nanotechnology for High Performance Fuel Cells" (HiPer-FC) project from the New Energy and Industrial Technology Development Organization (NEDO) of Japan, and a Scientific Research Grant (B24350093) from the Ministry of Education, Science, Sports, and Culture of Japan.

References

a. Fuel Cell Nanomaterials Center, University of Yamanashi, Miyamae 6-43, Kofu, 400-0021, Japan.
b. Clean Energy Research Center, University of Yamanashi, Takeda 4, Kofu, 400-8511, Japan.
c. Mitsui Mining and Smelting Co., Ltd., Haraichi 1333-2, Ageo, Saitama, 362-0021, Japan.

*Author to whom correspondence should be addressed. Phone: +81-55-220-8620; Fax: +81-55-254-0371; E-mail: m-watanabe@yamanashi.ac.jp

1 T. Yoda, H. Uchida and M. Watanabe, *Electrochim. Acta* 2007, **52**, 5997-6005.
2 T. Aoki, A. Matsunaga, Y. Ogami, A. Maekawa, S. Mitsushima, K. Ota and H. Nishikawa, *Power Sources* 2010, **195**, 2182-2188.
3 D. H. Lim, W.J. Lee, N. L. Macy and W. H. Smyrl, *Electrochem. Solid-State Lett.* 2009, **12,** B123-B125.
4 S. Yin, S. Mu, M. Pan and Z. Fu, *J. Power Sources* 2011, **196**, 7931-7936.
5 B. Avasarala and P. Haldar, *Electrochim. Acta* 2010, **55**, 9024-9034.
6 Y. Liu and W. E. Mustain, High Stability, *J. Am. Chem. Soc.* 2013, **135**, 530-533.
7 S. Keerthi, H. Rob, C. Stephen, Y. Siyu and Z. Jiujun, *Electrochim. Acta* 2012, **59**, 538-547.
8 B. Wickman, M. Wesselmark, C. Lagergren and G. Lindbergh, *Electrochim. Acta* 2011, **56**, 9496-9503.
9 A. Ignaszak, C. Song, W. Zhu, J. Zhang, A. Bauer, R. Baker, V. Neburchilov, S. Ye and S. Campbell, *Electrochim. Acta* 2012, **69**, 397-405.
10 M. K. Jeon, K. R. Lee, W. S. Lee, H. Daimon, A. Nakahara and S. I. Woo, *J. Power Sources* 2008, **185**, 927 – 931.
11 W. Yao, J. Yang, J. Wang and Y. Nuli, *Electrochem. Commun*. 2007, **9**, 1029-1034.
12 T. Ioroi, H. Senoh, S. Yamazaki, Z. Siroma, N. Fujiwara and K. Yasuda, *J. Electrochem. Soc.* 2008, **155**, B321-B326.
13 T. Ioroi, Z. Siroma, N. Fujiwara, S. Yamazaki and K. Yasuda, *Electrochem. Commun.* 2005, **7**, 183-188.
14 T. Ioroi, T. Akita, M. Asahi, S. Yamazaki, Z. Siroma, N. Fujiwara and K. Yasuda, *J. Power Sources* 2013, **223**, 183-189.
15 F. Takasaki, S. Matsuie, Y. Takabatake, Z. Noda, A. Hayashi, Y. Shiratori, K. Ito and K. Sasaki, *J. Electrochem. Soc.* 2011, **158**, B1270-B1275.
16 A. Masao, S. Noda, F. Takasaki, K. Ito and K. Sasaki, *Solid-State Lett.* 2009, **12**, B119-B122.
17 M. Dou, M. Hou, D. Liang, W. Lu, Z. Shao and B. Yi, *Acta* 2013, **92**, 468-473.
18 M. P. Gurrola, J. Gutie´rrez, S. Rivas, M. Guerra-Balca´zar, J. Ledesma-Garcı´a and L. G. Arriaga, *Int. J. hydrogen Energy*, in press.
19 K. Kakinuma, Y. Chino, Y. Senoo, M. Uchida, T. Kamino, H. Uchida and M. Watanabe, *Electrochim. Acta* 2013, **110**, 316-324.
20 K. Kakinuma, Y. Wakasugi, M. Uchida, T. Kamino, H. Uchida and M. Watanabe, *Electrochemistry* 2011, **79**, 399-403.
21 Y. Wang, S. Song, V. Maragou, P. K. Shen and P. Tsiakaras, *Appl. Catal. B* 2009, **89**, 223-228.
22 S. Y. Huang, P. Ganesan and B. N. Popov, *Appl. Catal. B*, 2011, **102**, 71-77.
23 N. R. Elezovic, B. M. Babic, V. R. Radmilovic, L. M. Vracar and N. V. Krstajic, *Electrochim. Acta* 2011, **56**, 9020-9026.
24 C. V. Subban, Q. Zhou, A. Hu, T. E. Moylan, F. T. Wagner and F. J. DiSalvo, *J. Am. Chem. Soc. 2010,* **132**, 17531-17536.
25 C. Zhang, H. Yu, Y. Li, L. Fu, Y. Gao, W. Song, Z. Shao and B. Yi, *Chem*. 2013, **701**, 14-19.
26 M. S. Saha, R. Li, M. Cai and X. Sun, *Solid-State Lett.* 2007 **10**, B130-B133.
27 K. Kakinuma, M. Uchida, T. Kamino, H. Uchida and M. Watanabe, *Electrochim. Acta* 2011, **56**, 2881-2887.
28 N. Riefler and L. Mädler, *J. Nanopart. Res.* 2010, **12**, 853-863.
29 M. Watanabe, M. Uchida and S. Motoo, *J. Electroanal. Chem.* 1986, **199**, 311-322.
30 M. Watanabe, M. Uchida and S. Motoo, *J. Electroanal. Chem.* 1987, **229**, 395-406.
31 M. Uchida, Y. Aoyama, M. Tanabe, N. Yamagihara, N. Eda and A. Ohta, *J. Electrochem. Soc.* 1995, **142**, 2572-2576.
32 Watanabe, M. Tomikawa and S. Motoo, *J. Electroanal. Chem.* 1985, **195**, 81-93.
33 M. Watanabe and S. Motoo, *J. Electroanal. Chem.* 1975, **60**, 259-266.
34 M. Watanabe and S. Motoo, *J. Electroanal. Chem.* 1975, **60**, 267-273.
35 R. D. Shannon, *Acta Cryst*. 1976, **A32**, 751 – 767.
36 J. F. Boyle and K. A. Jones, *J. Electron. Mater.* 1977, **6**, 717-733.
37 N. Barsan and U. Weimar, *J. Electroceram.* 2001, **7**, 143-167.
38 A. Fujishima, X. Zhang and A. D. Tryk, *Surf. Sci. Rep.* 2008, **63**, 515-582.
39 C. Coutanceau, M. J. Croissant, T. Napporn, C. Lamy, *Electrochim. Acta* 2000, **46**, 579-588.
40 H. Yano, T. Akiyama, P. Bele, H. Uchida and M. Watanabe, *Phys. Chem. Chem. Phys.* 2010, **12**, 3806-3814.